

## Chapter 2

# Fundamentals

**Abstract** In this chapter, we firstly introduce the application of optical technology in cellular imaging. Then, we will introduce the fundamentals about analysis and classification of HEP-2 cell images. Our works focus on the efficient feature extraction for staining pattern classification of HEP-2 cells. There are countless features existed for image classification. Firstly we refer some widely used features for describing staining patterns, then we will introduce some fundamental classifiers for staining patterns classification.

### 2.1 Optical Systems for Cellular Imaging

This section introduces application of optical technology in cell imaging, highlighting the basic principle and main features of a list of microscopic techniques, including laser scanning confocal microscope, multi-photon fluorescence imaging, total internal reflection fluorescence microscopy, near-field scanning optical microscopy imaging, and optical coherence tomography. To an extent, these optical imaging techniques have demonstrated characteristics of non-invasive, non-ionizing radiation, and various operating modes, providing a variety of real-time quantification of cellular properties and playing a decisive role in the life science research. Applications of optical imaging technology in life science have a history of over two hundred years, and microscopic analysis has been playing an important role in the biomedical field. Recent progress in laser technology has made remarkable achievements in tissue optics, spectroscopy, imaging technology, optical diagnostics and treatment technology. In many of state-of-the-art biomedical systems in nano-science, such as microarray biochips and one-drop blood diagnosis, optical imaging is a core part that plays a pivotal role in analysis. A new discipline-biomedical photonics has formed, focusing on optical technology in biomedicine.

### ***2.1.1 Laser Scanning Confocal Microscope***

Optical scanning confocal microscope has gained decades of continuous improvement for its high resolution and penetration capability into tissues. In 1957, Marvin Minsky clarified the basic principles of scanning confocal microscopy techniques for the first time. But it did not really become available in scientific research until 1985 with the rapid development of computer, laser and image processing technology. Wijnadts Van Resaint first succeeded in obtaining a cross-section of the optical probe with a fluorescent labeled biological material, demonstrating confocal fluorescence microscopy has an ability to reject defocused light to obtain three-dimensional image of biological samples. Within the next two years, Oxfordshire company, which was acquired by Bio-Rad Laboratories later, produced the first commercial laser scanning confocal microscopy, which became widely used in many fields. With high resolution, it implemented observation of biological processes within living tissue. Confocal microscopy has the ability to make chromatography, obtaining fluorescence image of internal fine structure of cells, or observing physiological signals and changes in cell morphology  $\text{Ca}^{2+}$ , pH value, the membrane potential at the subcellular level, etc. These advantages make laser scanning confocal microscope a powerful tool for clinical diagnosis, biomedical biochemistry, cell biology, reproductive biology and neurology [11, 19, 21, 23, 24, 34, 37, 42, 46, 50, 57, 60].

#### **2.1.1.1 Fluorescent Probe and Laser Scanning Confocal Microscopy Imaging Techniques**

Confocal laser scanning microscopy is a powerful tool for in situ observation and analysis in cell biological research involving fluorescent probes. There is a class of dyes in biological stain that can be excited by ultraviolet or blue-violet light and other short-wavelength light and emit fluorescence, which is called fluorescent dyes, also known as fluorescent pigment. Now some applied dyes can also be excited by longer wavelength light and produce longer wavelength fluorescence, these fluorescent dyes are often referred to as fluorescent probes. Fluorescent staining has the most significant advantages of high sensitivity in observation. The concentration of non-fluorescent dye usually needs to be 1% or higher to make the cells to carry with visible color. Fluorescent dyes, such as fluorescent yellow stained with a concentration of  $10^{-5}\text{M}$ , can stimulate visible fluorescence with ultraviolet excitation. Fluorescent dyes can produce a desired dyeing effect with concentration of from  $10^{-4}\text{M}$  to  $10^{-5}\text{M}$ .

Fluorescent dyes may be divided into three categories according to their chemical reactivity of fluorescent probes: (1) Alkalinity fluorescent dye, which contains alkaline chromophore ionized in acidic solution, with fluorescent color being cationic ions. Acridine dyes such as acridine yellow can stain cells by binding to DNA and RNA, mainly through embedded in the DNA double helix structure. Ethidium bromide stains by embedding in DNA, emitting red fluorescence under irradiation of

ultraviolet light. (2) Acid fluorescent dyes that contain acidic chromophore, ionized in alkaline solution, while fluorescent color ions being anions. (3) Neutral fluorescent dye, a compound dye that is a mixture of acidic and alkalinity fluorescent dye.

Depending on different applications, the fluorescent probes can further be divided into many categories, including cell active probes, probe organelles, membrane fluorescence showing needles, accounting probe, the membrane potential probes, ion probe, pH probe, reactive oxygen probes, immunofluorescence probes, probe caged compound, cytoskeletal protein fluorescence probes. It is essentially important to choose a fluorescent probe according to requirements of analysis and application conditions.

On the other hand, there has been a new nano-material called “quantum dots”, which have gradually become the latest fluorescent probes for their remarkable optical efficiency and exhibited a unique advantage in the field of cellular imaging technology. Study scope of quantum dots involves multiple disciplines. Even its name varies in different field of research, For example, colloid chemists attributed it to the colloidal particles (colloid particle), and material scientist named it nanocrystals (nanocrystal); while the solid-state physicists named it quantum dots due to confinement of electrons in a region of tens nanometer scale. Common semiconductor quantum dots are divided into quantum dots of iv Group (Si, Ge), iii–v Group (InAs, GaSb), and Group II–VI (ZnTe, CdSe, CdS, ZnO). iv Group and iii–v Group quantum dots are fabricated using photolithography, selective epitaxial growth and self-assembly method. Group ii vi diselenide, e.g. CdSe, has excellent fluorescence properties because of its wide bandgap and direct band gap characteristics. Fluorescent probe label plays an important role in cell microscopic imaging, as such, ii–vi Group quantum dots have attracted wide attention in this field [4, 7, 9, 22, 33, 35, 36, 38, 49, 52, 58].

Group ii–vi quantum dots have remarkable advantages over conventional organic fluorescent dyes on the following aspects: (1) as a multi-electron system, absorption coefficient of the quantum dots is much higher than that of a single molecule, with a magnitude of absorption coefficient reaching  $10^5 \text{ L} \cdot \text{mol}^{-1} \cdot \text{cm}^{-1}$  under visible light or ultraviolet light excitation, which makes its fluorescence emission intensity much higher than the organic dye; (2) by changing the material ratio and size of the quantum dot, the fluorescence emission wavelength can cover a wide spectral range from 400 nm to 2  $\mu\text{m}$ ; (3) in contrast to organic dye molecules that have a narrow excitation spectrum, quantum dots have a wide and continuous excitation spectrum and there is a quantum confinement emission peak (the longest wavelength can excite quantum dot to emit fluorescent light), any light whose wavelength is shorter than the quantum confinement peak can efficiently excite the quantum dots, so it is possible to use a single wavelength light source to excite quantum dot with different composition and sizes, making them emit different colors of fluorescence for simultaneous monitoring or distinguishing bio-processes; (4) fluorescence emission peak of quantum dots in an organic dye has a narrow and symmetrical peak, with a half-width of only 1/3 of that of fluorescent dyes, and has no tail in long-wave side; (5) the fluorescence lifetime is longer (about several hundred nanoseconds), fluorescence bleaching rate is only 1/100 of rhodamine 6G (a popular red fluorescent

dye), therefore it can be used for a long lifetime fluorescence microscopy experiments with a great potential to substitute conventional organic dyes as a new biological fluorescent probe.

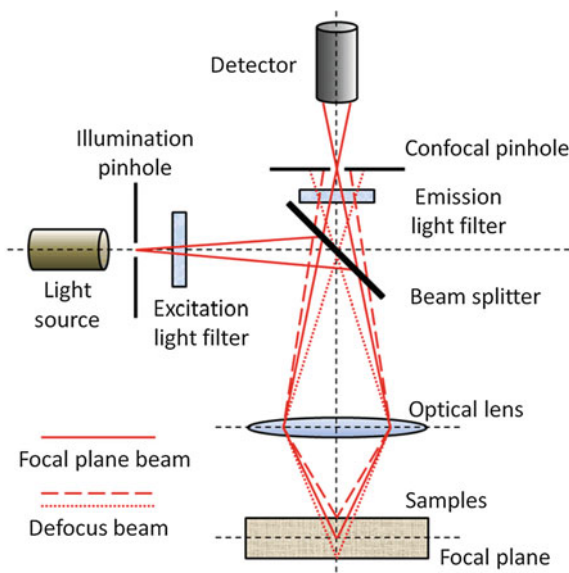
Two papers by Alivisatos and Nie respectively published in the same issue of *Science* in 1998 debuted the application of quantum dots in the biomedical fields, firstly reporting quantum dots in cell imaging as a fluorescent probes instead of conventional dyes [9]. The usage of quantum dots for highly sensitive cellular imaging has found major advances over the past decade [51]. The improved photostability of quantum dots, for example, allows the acquisition of many consecutive focal-plane images that can be reconstructed into a high-resolution three-dimensional image [59]. Another application that takes advantage of the extraordinary photostability of quantum dot probes is the real-time tracking of molecules and cells over extended periods of time [13]. Antibodies, streptavidin [27], peptides [3], DNA [18], nucleic acid aptamers [16], or small-molecule ligands [33] can be used to target quantum dots to specific proteins on cells. Researchers were able to observe quantum dots in lymph nodes of mice for more than 4 months [6].

Semiconductor quantum dots have also been employed for in vitro imaging of pre-labeled cells. The ability to image single-cell migration in real time is expected to be important to several research areas such as embryogenesis, cancer metastasis, stem cell therapeutics, and lymphocyte immunology.

### 2.1.1.2 Fundamentals of Confocal Laser Scanning Microscopy

Figure 2.1 shows a description of the basic principles of confocal laser scanning microscope imaging. The excitation light goes through illumination pinhole and form a point light source, reflected by a beam splitter by means of exciting filter, focused by the microscope objective into the three-dimensional sample. By scanning in the direction perpendicular to the optical axis in the  $xy$  plane (focal plane), fluorescence emitting from illuminated region on the focal plane and on the top and bottom of the focal plane is collected by objective with the beam splitter and emission filter. There is a confocal pinhole in front of the detector, the illumination pinhole and confocal pinhole is conjugate with respect to the focal plane of the objective lens, so that only the fluorescence emitted from the focal plane can be focused to a confocal pinhole and goes through the pinhole and reaches the detector either PMT or CCD. Points above or below the focal plane cannot be imaged into the detect pinhole, the light emitted outside of the focal plane is blocked by the pinhole, it contributed very little to confocal images. Thus the confocal images substantially only obtain light information from the focal plane, namely acquired a 2D image sampled by the focal plane. If gradually adjusting the position of the longitudinal axis of the sample, multiple tomographic image of the sample can be generated and each cross-sectional image of cell or tissue can be clearly displayed. This imaging method is called a confocal scanning microscope tomography. With three-dimensional image reconstruction technique, a high resolution three-dimensional image of the sample can be provided, as in many commercial instruments.

**Fig. 2.1** Imaging principle of confocal laser scanning microscopy



### 2.1.1.3 Characteristics of Confocal Laser Scanning Microscope

If the pinhole is removed from a laser scanning confocal microscope imaging system, the defocused light (light from off focal planes) can reach the detector, the resolution in the depth direction will be greatly reduced, then the non-confocal optical microscope would be no much different from an ordinary microscope. So the most fundamental difference between confocal laser scanning microscope and the ordinary microscope is that there is a pair of conjugate pinholes to limit received light rays only from focal plane, thus largely eliminating the blur effect of defocused light. Another remarkable difference lies on the fact that laser scanning system can acquire an extremely low aberration as the whole optical imaging system needs only to deal with point-to-point imaging, instead of a complete field of view, which requires a sophisticated optical aberration reduction for system design. Compared with a general-purpose optical microscope, a confocal laser scanning microscope has the following characteristics:

- (1) Scattering background of confocal laser scanning microscope is lower than normal optical microscope, resulting in a high image contrast and detection sensitivity.
- (2) Three-dimensional imaging can be reconstructed from layer to layer image data, forming a light-ray tomography through line by line, point by point three-dimensional scanning, completely different from computed tomography method. Image data stored in the computer allows display any two-dimensional cross-sectional or perspective view of three-dimensional tomography.

- (3) Utilization of laser light source provides a small size and high brightness illumination light spot on focal plane. Monochromatic laser light essentially eliminates chromatic aberration of the system. With advances in laser technology, more and more types of lasers have been fully able to meet the needs of biomedical research sample.

Commercialization of laser scanning confocal microscope are usually equipped with powerful image processing software, realizing functions of positioning of multiple fluorescent labeling, optical sectioning, 3D reconstruction, time series scanning and other quantitative analysis.

#### **2.1.1.4 Application of Confocal Laser Scanning Microscope**

Being equipped with advanced data acquisition, recording and processing algorithm, laser scanning confocal microscope is becoming one of the most important molecular cell biology analytical instrumentation in life sciences research, including observing the structure of living cells and specific molecules, ions of biological histological changes, quantitative analysis, and real-time quantitative determination of bio-systems, which has derived a number of new technologies and new methods such as adherent cell sorting, laser cell microsurgical techniques, fluorescence recovery after photo-bleaching technique, intercellular communication, cell membrane fluidity measuring technology and photo-activation.

Laser scanning confocal microscopy has been widely used in the fields of biology, biochemistry, physiology, pharmacology, pathology, genetics and immunology and embryology science, environmental medicine and nutritional science. Some of examples include: investigation of internal element of the insect digestive tract, the enteric valve of Apicomitinae [26], and quantum dots labeled three-dimension imaging of nanofibrous structure [5].

#### **2.1.2 Multi-photon Fluorescence Imaging**

Conventional fluorescence microscopy techniques are based on single-photon excitation fluorescence, in which a fluorescent molecule absorbs a photon, transiting from the ground state to an excited state, followed with emission of a long wavelength photon by transiting to the ground state after the energy relaxation. The photon energy of excitation light used here must be higher than that of the emitted fluorescence wavelength for energy conservation. If long-wavelength photons to excite the fluorescent molecule, it will not produce fluorescence. In 1931, Maria Goppert-Mayer predicted that if one photon does not have enough energy to excite the fluorescent molecule, but in a short time to encounter a second or more photons, the same molecule can simultaneously absorb two or more photons, each of the absorption produces the molecule excitement with an equivalent energy of the absorbed photon. Conse-

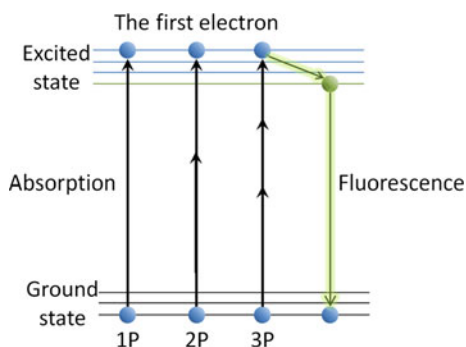
quently, the fluorescent molecule, after gaining sufficient photon energy, will also fluoresce after relaxation. This multiphoton excitation process, was not observed until the 1960s when two-photon excited fluorescence was first discovered in  $\text{CaF}_2:\text{Eu}^{3+}$  by Kaiser and Garret [34], there-photon excited fluorescence was observed and the three-photon absorption cross section for naphthalene crystals was estimated by Singh and Bradley [35].

As shown in Fig. 2.2, multiphoton fluorescence involves the absorption of multiple photons to an excited electronic state followed by the relaxation of the molecule to the ground electronic state through the emission of a single photon. The wavelength of the emitted photon is approximately equal to the excitation wavelength divided by the number of photons absorbed.

Two-photon excitation wavelength is twice single-photon excitation wavelength. For example, to excite the fluorescent probe Indo-1 with  $\text{Ar}^+$  laser, we use 351 nm laser, while two-photon excitation is necessary to use 700 nm laser. Despite there is a difference between single-photon and multi-photon excitation process, the fluorescence emission spectra are identical. That is, the multi-photon technology can detect ultraviolet fluorescent probe without the use of an ultraviolet light source. But to achieve multi-photon excitation, it usually requires ultra-fast femtosecond laser pulses to produce a high density of photons focused on suitable fluorescent medium, and induce multi-photon transition with a sufficiently high probability, due to the fact that the probability that more than one photon can be absorbed simultaneously scales with intensity raised to the  $n$ th power where  $n$  is equal to the number of photons absorbed. Thus the multi-photon excitation has high spatial local characteristics, only samples in the center area of focus can absorb enough photons to give off fluorescence, which naturally reduces size of emission spots on sample upon laser illumination. Based on this principle, multi-photon excitation can obtain clearer three-dimensional fluorescence image than the single-photon confocal (Figs. 2.3 and 2.4).

In addition, multi-photon fluorescence excitation uses red or infrared light, which minimizes scattering in the tissue. Further the background signal is strongly suppressed. Both effects lead to an increased penetration depth for these microscopes, typically 5–20 times deeper than other types of fluorescent microscopes. Two-photon

**Fig. 2.2** Single photon versus multi-photon excitation



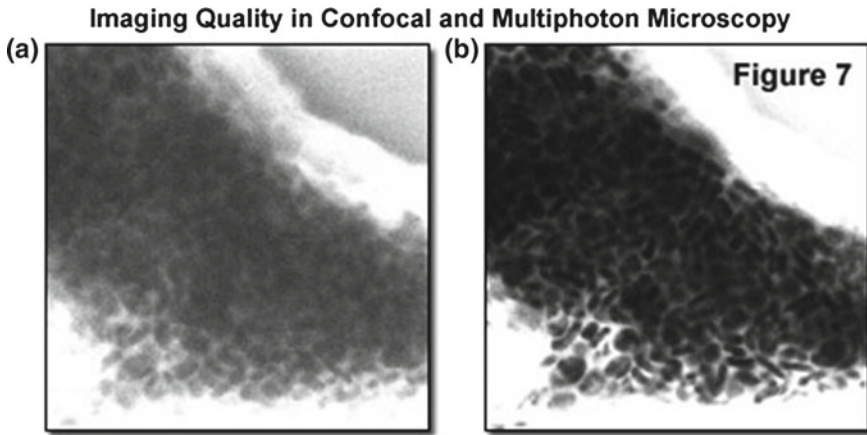


**Fig. 2.3** (a shark choroid plexus stained with fluorescein) provide a comparison of confocal and two-photon microscopy imaging quality [41]

excitation can be a superior alternative to confocal microscopy due to its deeper tissue penetration, efficient light detection, and that not only greatly reduces the phototoxicity of cells, but also extends the observation time of living organisms [8, 15, 20, 45, 55].

Single-molecule biophysical approaches to live-cell studies based on fluorescence imaging have greatly enriched our knowledge on the behavior of single biomolecules in their native environments and their roles in cellular processes [61]. And it can detect a variety of small molecules in vitro and allow imaging of the dynamic changes and cell-to-cell variation in the intracellular levels [43] (Fig. 2.5).

### 2.1.3 Total Internal Reflection Fluorescence Microscope

#### 2.1.3.1 The Principle of Total Internal Reflection

According to the principle of geometrical optics, when light in a medium with a higher refractive index reaches a boundary with a medium of lower refractive index, the wave will in general be partially reflected at the boundary surface, and partially refracted. With the increase of the angle of incidence, the intensity of the reflected light gradually increases and the intensity of the refracted light decreases. When the incident angle increases to angle  $\theta_c$ , the refraction angle is  $90^\circ$ . Then refraction of light passing the boundary between two media and the intensity closes to zero. When the incident angle  $\theta_i > \theta_c$ , refracted light no longer exists, the incident light is totally reflected. This phenomenon is called “total internal reflection” (TIR). When



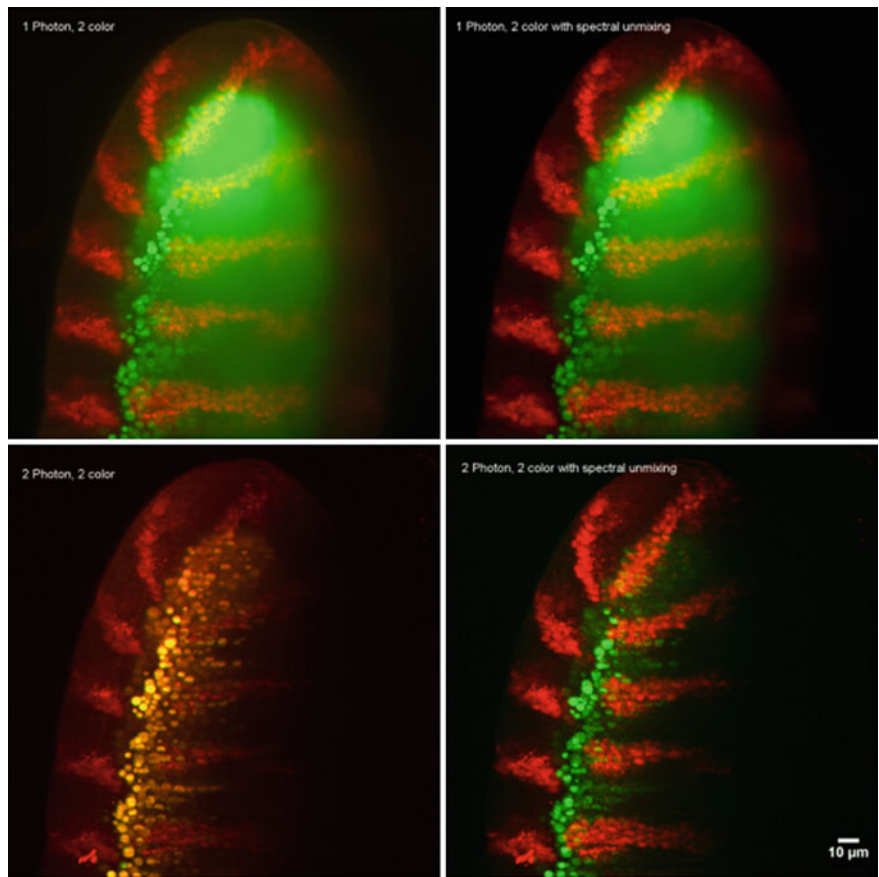
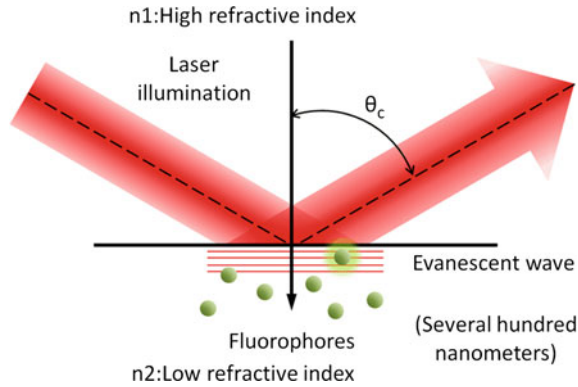


**Fig. 2.4** Comparison of images acquired by 2-photon process with that by 1-photon process under multiple color conditions [42]

**Fig. 2.5** Fluorophore excitation near surface by total internal reflection



refraction angle is  $90^\circ$ , the angle of incidence  $\theta_c$  called the “critical angle” or “total internal reflection angle.”

In the case of TIR, most of the light is reflected along the direction of the reflected light. Only a small portion of the reflected light propagates through a parallel interface of the surface and forms the electromagnetic field near the interface of the medium. This field is called the evanescent field, which decays exponentially with the increase of propagation distance, so in a very short distance (about a few hundred nanometers) the evanescent field will disappear. It is precisely that the energy can only excite the fluorescent probes close to the interface thanks to the nature of evanescent field, thus realizing the detection of single fluorescent molecule and researching on molecular interactions. This is very beneficial to the study of the characteristics of the cell membrane and other membrane structure.

### 2.1.3.2 Total Internal Reflection Fluorescence Microscopy (TIRFM)

Generally it is not difficult to realize the excitation of fluorescence probe molecules on the sample surface by using the evanescent field based on TIR, and there are many ways to choose. At the beginning of the studies of the, there has been widespread using prism or hemisphere combined with parabolic reflector to realize the TIR. This makes the instrument structure relatively complex, and prism quality and calibration requirement is high. Improved designs paid attention to the objective lens of the microscope in the process of seeking a new implementation method. Through constant improvement in design, the objective lens of total internal reflection microscopy that can be installed directly on the general fluorescence microscope appeared in the year 2000, making it extremely convenient to obtain total internal reflection fluorescence images. Its working principle is shown in Fig. 2.6. In addition to the difference of the light on the transmission between the other objective lens, its numerical aperture is greater than 1.38. The experimental results show that the greater the numerical aperture, the higher the image quality.

### 2.1.3.3 The Application of TIRFM

TIRFM only excites the fluorescent probe molecules near the interface, and the molecular away from the interface cannot obtain enough energy to generate fluorescence radiation. Figure 2.7 compares the different images of the same sample observed by TIRFM and ordinary fluorescence microscope. The fluorescence image obtained by TIRFM has a higher image contrast, suitable for the analysis of emitting mechanism.

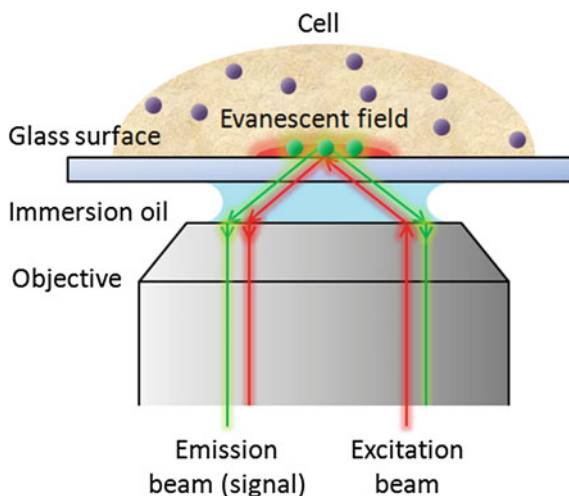


**Fig. 2.6** Schematic of total internal reflection fluorescence microscope

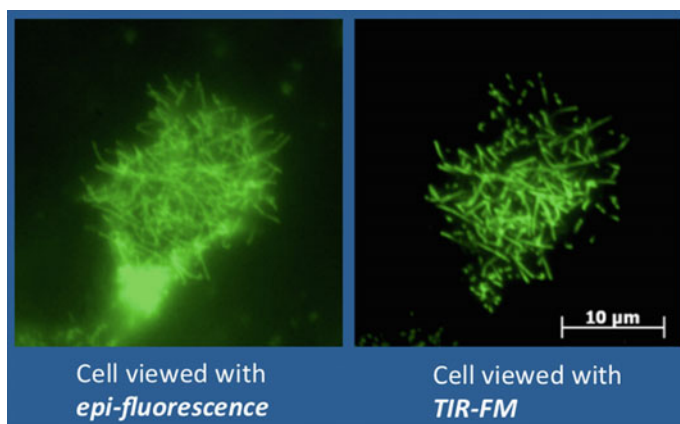


**Fig. 2.7** Comparison of images by TIRFM and ordinary fluorescence microscope [52]

### 2.1.4 Near-Field Scanning Optical Microscopy Imaging Technology

Near-field scanning optical microscope (also known as NSOM/SNOM) currently has the highest optical resolution. The literature reported its resolution can reach 10 nm and normally the resolution can be better than 50 nm. And previous optical microscope, even the confocal laser scanning microscope, the general spatial resolution of which can only up to 250 nm due to Ernst Abbe diffraction limit, namely  $d = 0.61/\lambda \sin \theta$ , where  $d$  is the smallest scale that an ordinary microscope can

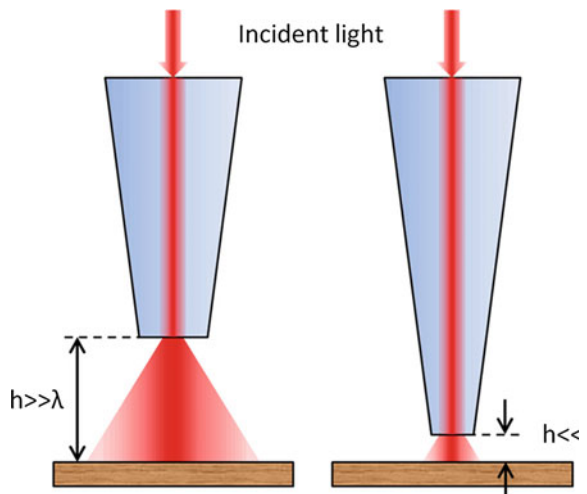
distinguish,  $\lambda_0$  is the wavelength of light,  $n$  is the refraction index of medium, and  $\theta$  is convergent angle of light beam [14, 17, 53, 54].

#### 2.1.4.1 Working Principle of the Near Field

In regard to a sample surface, its optical information can be roughly divided into near field information (less than a light wavelength range) and the far field information (more than a light wavelength range). Near field information contains more of the high frequency components than that in the far field, which can reveal more fine surface structure. But the near field information decays exponentially with the increase of propagation distance, it is difficult to obtain this information by using the general methods. Near-field optical microscope is a tool to collect the high frequency information. Although the near-field scanning optical microscope is an optical microscope, it does not have a lens system. It uses an extremely sharp beam probe to collect optical information on the surface of the sample. Usually we use a microscope to observe samples in a distance at least several wavelengths (Fig. 2.8a), which can only see the image of the far field. If we decrease the distance between collect lighting and the sample on the surface ( $\ll \lambda$ ), it is possible to acquire an image with high frequency information, namely high resolution (Fig. 2.8b).

Back in 1928, Synge proposed that if there is a hole in an opaque plate with backward lighting, with the hole scale being far less than wavelength, then the scale of the light through the plate depends on the size of the hole. If the plate is closely near the surface, the light through the hole can implement imaging of the sample surface, so as to realize the breakthrough of the image resolution restricted by diffraction limit. But at that time the hole production, lighting and sample controlling problems are hard to verify his idea, until 1972 Ash and Nichols using microwave confirmed his

**Fig. 2.8** Comparison of focusing beam spread in imaging process: **a** far-field, **b** near-field



prediction. Since then, Winfried Denk, inspired by scanning tunneling microscope (STM), realized the sub-wavelength visible light detection in IBM laboratory at Zurich in 1982 for the first time. Aaron Lewis from Cornell University also realized near-field detection independently by using laser and a probe drawn by glass capillary to propagate light signals. By keeping the distance between the probe and the sample on the scale of a few nanometers, he scanned the sample surface point by point to recover the optical image of the sample. These creative work of near-field scanning optical microscope provided possibility in the application of scientific research and started a widely research of near-field scanning optical microscope since then.

Studies found that several conditions must be met in order to obtain satisfactory near-field optical images. First, using a laser as light source to supply sufficient incoming light intensity, as the near field optical signal is so weak that it is easy to drown in the background noise. For this reason, oftentimes lock-in amplification is utilized to resolve signal out of noise, too. Second, the scale of the probe needs to be at the nanometer level to effectively detect near-field optical signal, otherwise it is difficult to guarantee a high resolution exploration. Third, the distance between the probe and the sample should be controlled within a few nanometers.

#### **2.1.4.2 The Characteristics and Classification of Near-Field Scanning Optical Microscope**

Near-field optic not only retains the advantages of ordinary microscopes, but also significantly increases resolution; some of these advantages can be simply summarized as the following:

- (1) the non-invasive, non-destructive scanning of sample surface, particularly suitable for biological sample, in-situ detection can be realized;
- (2) a wealth of method to improve or adjust image contrast by placing the samples through light absorption, reflection, scattering, polarization, phase and the spectral selection, allowing a full range of rich information for the researchers.
- (3) detection sensitivity can reach as high as 1photon/sec;
- (4) capable of achieving 10 nm optical resolution;
- (5) able to detect spectral information as well as lifetime of a single fluorescence molecule;
- (6) By point by point scanning near-field scanning optical microscope can obtain the morphology image of the sample along with 2D optical image at the same time.

Near-field optical microscopy is able to break through the diffraction limit through using a nanoscale optical probe to disturb the evanescent wave close to sample surface, which turns the evanescent wave into detectable propagation wave, so as to improve the resolution of the image. According to the type of probes used, near-field optical microscopes can be divided into two kinds: the probe allows transmitting light signals, and is connected to a light source or detector, usually made by stretching optical fiber or glass capillary into a conical tip, coated with a thin reflective metal

layer, often aluminum. The end of the fiber is an uncoated small pinhole through which an evanescent light wave can pass. The diameter of the hole is often 50–100 nm. The transmission decreases very rapidly with diameter (approximately the 6th power), in industry this type of optical fiber based probe is also named as SNOM probe (scanning near-field optical microscope probe), usually fabricated by stretching an optical fiber under electric coil heating. Another kind probe is an opaque conical needle without optical aperture, only perturbing the near field with its sharp tip. During scan, intensity change in reflected irradiation laser beam is picked up and computer processed to produce image; those probes are mostly made of semiconductor (e.g. silicon) or metal, and often used with AFM simultaneously. Figure 2.9 shows the imaging schemes using two types of probes.

As for near-field scanning optical microscopes with light-guided probes are further classified into two configurations that light source and detector are located: one kind is reflective near-field scanning optical microscope, the light source and detector are on the same side of the sample, and the probe can be either light source or detection device. It is suitable for the research of metal, thicker, opaque or samples of the insulation, while the other is a transmission near-field scanning optical microscope: the light source and detector on the opposite side of the sample. Probes are only used for illumination, suitable for transparent thin samples, where transmitted near-field signals are collected.

Recently near-field scanning optical microscopes have seen some new hybrids in practical applications, such as the combination of scanning near-field optical microscope with an atomic force microscope (AFM) to become a multifunctional system whose resolution reached 35 nm, and a near-field scanning optical microscope on which a sensitive polarization detector is installed to detect local magneto-optic effect with a high lateral resolution.

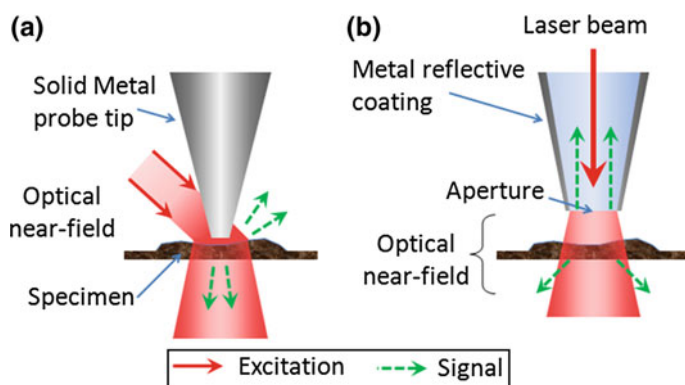


**Fig. 2.9** Two near-field imaging schemes: **a** solid metal tip probe, **b** SNOM probe

### 2.1.4.3 The Application of Near-Field Scanning Optical Microscope

With the improvement of resolution and image quality of the near-field scanning optical microscope, the scope of its application is becoming more and more widely, from the single molecule fluorescence spectrum detection to the film and materials research, especially attracted the attention of people in the field of biological medicine and bio-chemistry.

The connections of near field scanning optical microscope with monochromator or optical multichannel spectrum analysis instrument produce a multi-functional system with spatial resolution and time resolution, provides possibilities for studying inhomogeneity of nanoscale samples through realizing the detection of spectrum from micro region of the sample. This trend of continuous improvement of the near-field scanning optical microscopy receives a strong attention in biology research. Combined Near field scanning optical microscopy together with fluorescence resonance energy transfer (FRET) not only provides high spatial resolution of sample topography and fluorescence image, but also increases longitudinal sensitivity for dynamic measurement at a single point by utilizing distance dependence FRET techniques; The use of ultrafast lasers to make the near-field scanning optical microscope to study ultrafast two-photon induced single molecule fluorescence; The combination of near field scanning optical microscopy and CLSM (confocal laser scanning microscope) can study the nucleus, DNA, the cell membrane and membrane protein fluorescence images, accurately determine the cell and the location of the organelles within the structure of proteins. This method also enables in-situ detection of samples in the liquid environment, imaging the myofibril with the fluorescent tag in the physiological saline. The structure of z-line protein of myofibril with antibody markers is easy to recognize in the near field fluorescence images. Successful observations include tobacco Mosaic virus, the salmonella flagella filaments in the water, bacteria and LB film [14, 17, 28, 29, 53, 54].

Despite that the near-field scanning optical microscope (NSOM) has achieved outstanding results in many field, various technical indicators are still under constant improvement, making it gradually become a powerful tool for life science research. A new form of aperture-type NSOM was proposed whose resolution was not determined by the resolution of the recovered image but the sharpness of the corners of the rectangular aperture and the step size of the scan, this feature of DNSOM (differential near-field scanning optical microscope) makes it potentially advantageous for nanometer-level imaging, especially when resolution and light throughput are at a premium [41].

### 2.1.5 Optical Coherence Tomography Technology

Since Huang et al. from the Massachusetts institute of technology at the United States published an article titled “technology of optical coherence Tomography (OCT)” on Science in 1991, OCT technology has been an active field of scientific research. OCT



can obtain high-resolution cross-sectional imaging of tissue microstructure. Similar to ultrasonic imaging, OCT uses infrared light waves to replace sound waves to focus beam into the tissue to measure at different axial and lateral position repeatedly, which obtain image information to get the two-dimensional backward scattering field or reflection images. OCT image reflects the structure of the tissue and cellular structure [1, 25, 30, 48, 63].

OCT technology combines the confocal, low coherence, optical heterodyne and scanning tomography and other technical advantages, which can realize real-time, non-invasive and in vivo detection. It has a high detection sensitivity and resolution: lateral resolution can reach 4–2 m, the longitudinal resolution can reach 10  $\mu\text{m}$ , far greater than the resolution of the X-ray photography. In the clinical imaging, OCT integrated with catheter or endoscopic can get high resolution imaging of the internal organs microstructure. Applications in medical include: imaging of articular cartilage, cardiovascular imaging, imaging of the esophagus, cervix imaging, retinal imaging, etc. It also can be used to measure the characteristic parameters of biological tissue and fluid velocity.

Based on low-coherence interferometry, Optical coherence tomography is typically employing near-infrared light, which allows penetration into tissue to collect scattering light from layers with different depths. OCT is coherent field tomography technology, its interference conditions are: (1) the frequency of the two beams is the same or very close to, namely light frequency difference is much smaller than the frequency of light used; (2) phase difference of two beams of light is a constant; (3) light polarization direction is not perpendicular to each other.

The center part of the OCT is a Michelson interferometer, as shown in Fig. 2.10. A coherent light source is fed into a  $2 \times 2$  optical fiber coupler, which connects to reference side (a mirror) and the signal side (sample to be tested), respectively. Mirror reflected light (the reference light) interferes with light backscattered from the sample (signal light) through the fiber coupler to produce interference signal, which is received by a detector. The intensity of the signal reflects the scattering (reflection)

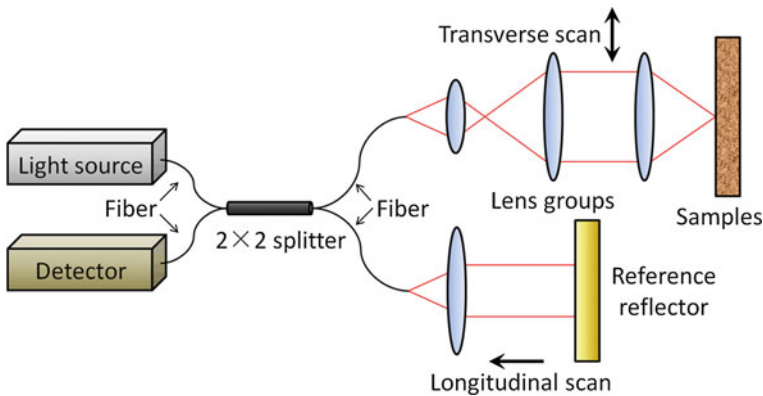


**Fig. 2.10** System schematic of OCT



strength of the sample, only the scattering signal from a particular sample depth is coherent with the reference beam due to a short coherent length of the light utilized, thus a high layer selectivity, or depth resolution is obtained. Tomographic resolution is directly determined by the coherence length of the light source, the shorter the coherence length, the higher the depth resolution. But the shorter the coherence length of the light source, the weaker its interference signal. In choosing a light source, one should consider a balance among the resolution, the optical properties of the sample, and appropriate light source coherence. To achieve the lateral resolution, output light beam needs to be focused down to micrometer size for 2D scanning. The performance of OCT imaging capability also depends on sensitive heterodyne detections and discrimination of scattered light from off-focal planes. By use of a PS-OCT system with an integrated retinal tracker, analysis of optimum conditions for depolarization imaging, data processing, and segmentation of depolarizing tissue in the human retina was realized [56].

## 2.2 Feature Extraction

Feature extraction is a very important issue in pattern recognition and classification. Suitable and discriminative features can efficiently present different contents in the image and offer strong supports for final classification. A large number of features have been proposed, however, we introduce some important and effective features applied for representing the staining patterns in this section. Roughly, we introduce the features from two aspects, i.e., low-level features and mid-level features.

### 2.2.1 Low-Level Features

We define the features describe image content from the primitive level as low-level features. It is a relative concept to the mid-level features obtained by using Bag-of-Words (BoW) framework.

#### 2.2.1.1 Local Binary Patterns

LBP [39] is initially proposed to describe textural features for a local region. It can be obtained by thresholding the gray value of the circularly symmetric neighbor pixels with that of the center pixel. The neighbors whose difference is positive are set as '1' while others are set as '0'. Then, these binary values are converted to a decimal number.

Let  $I$  be a grayscale image and  $I(x, y)$  be a gray value at location  $(x, y)$  in  $I$ . Then LBP at location  $(x, y)$  is defined as

$$LBP_{P,R}(x, y) = \sum_{i=0}^{P-1} 2^i \text{sign}(I(x_i, y_i) - I(x, y)), \quad (2.1)$$

$$\text{sign}(x) = \begin{cases} 1, & \text{if } x \geq 0 \\ 0, & \text{otherwise.} \end{cases} \quad (2.2)$$

where  $I(x_i, y_i)$  is the gray value of  $P$  equal spaced pixels on a circle of radius  $R$  around center pixel  $(x, y)$  and  $(x_i, y_i)$  is the location of neighbors given by  $(x_i, y_i) = (x + R \cos(2\pi i/P), y + R \sin(2\pi i/P))$ . If the neighbors do not fall in the center of pixels, their gray values should be estimated by interpolation [40]. Figure 2.11 illustrates the procedure to obtain  $LBP_{P,R}$  value with different  $(P, R)$ .

The  $LBP_{P,R}$  produces  $2^P$  different output values, therefore we can calculate the  $LBP_{P,R}$  value for each pixel of an image and build a histogram with  $2^P$  bins as the image descriptor. The original  $LBP_{P,R}$  achieves invariance against any monotonic transformation and the scaling of the gray-scale.

To achieve rotation invariance, a unique identifier is assigned to each rotation invariant LBP [40], which is formulated by

$$LBP_{P,R}^i(x, y) = \min\{\text{ROR}(LBP_{P,R}(x, y), s) | s = 0, 1, \dots, P-1\}, \quad (2.3)$$

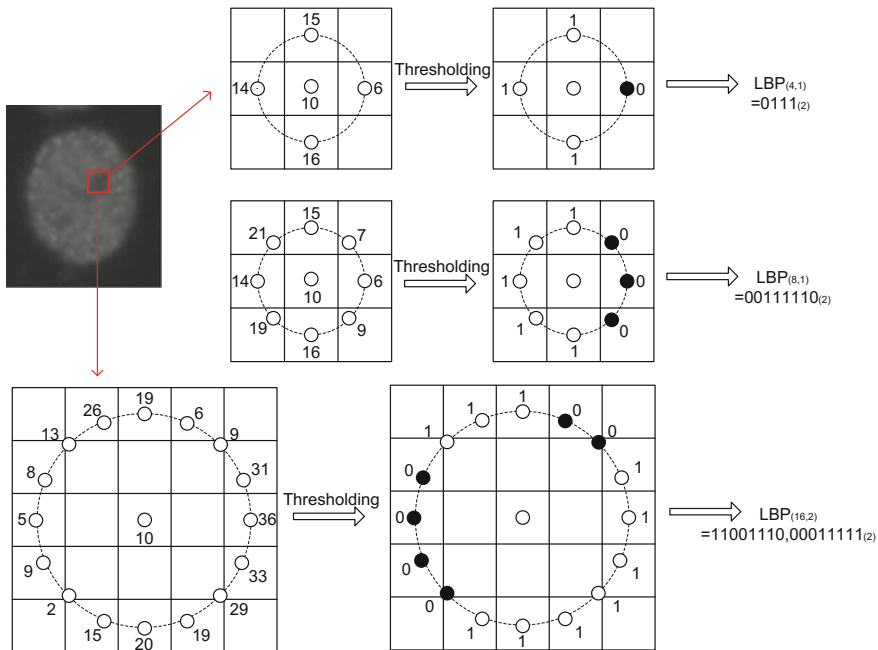


**Fig. 2.11** Local binary patterns with different  $(P, R)$ s:  $(4, 1)$ ,  $(8, 1)$  and  $(16, 2)$

where  $ROR(x, s)$  performs circle-right-shift on the binary number  $x$   $s$  times. For example,  $LBP_{P,R}$  values 10000100b, 00100001b and 01000010b all map to the unique value 00100001b.

Another extension of original LBP called “uniform” patterns [40]. A uniformity measure  $U(LBP_{P,R})$  is introduced to denote the times of spatial transitions (bitwise 0/1 changes) in the LBPs. For instance, pattern 00000010b and 00111000b have  $U(LBP_{P,R})$  value of 2; pattern 01100010b have  $U(LBP_{P,R})$  value of 4. Uniform LBP assigns different label to each “uniform” pattern and gives a unique number to all the “non-uniform” patterns. The uniform LBP has  $P(P - 1) + 3$  different values. Figure 2.12 shows 58 different “uniform” patterns of  $(8, R)$  neighborhood. Each “uniform” pattern has an unique label from 1 to 58 and all “non-uniform” patterns (there are 198 patterns are “non-uniform”) are assigned the same label 59. Let  $U_P(i, j)$  be the label for a “uniform” pattern, where  $i$  is the number of ‘1’ in the pattern (row number in Fig. 2.12) and  $j$  is the rotation degree (column number in Fig. 2.12) The uniform LBP can be formulated as

$$LBP_{P,R}^{u2}(x, y) = \begin{cases} U_P(i, j), & \text{if } U(LBP_{P,R}) \leq 2 \\ P \times (P - 1) + 3, & \text{otherwise.} \end{cases} \quad (2.4)$$

$$U_P(i, j) = \begin{cases} 1, & i = j = 0, \\ (i - 1) \times P + j + 2, & 1 \leq i \leq P, 0 \leq j \leq P - 1, \\ P \times (P - 1) + 3, & i = P, j = 0. \end{cases} \quad (2.5)$$

The “uniform” patterns provide stronger ability of discrimination in comparison to including all patterns, because they have different statistical properties [40, 44]. Most of the LBPs in natural images are uniform. The proportion of “non-uniform” patterns is so small, therefore the estimation of their probabilities is unreliable. Meanwhile, “uniform” patterns are more stable and only considering “uniform” patterns makes the distribution estimation more reliable.

To improve the capability of rotation invariance and elevate the discrimination, some rotation invariant patterns with low occurrence frequencies, i.e., “non-uniform” patterns of rotation invariant LBPs, are eliminate. The improved rotation invariant texture feature can be defined as [40]

$$LBP_{P,R}^{riu2}(x, y) = \begin{cases} \sum_{i=0}^{P-1} \text{sign}(I(x_i, y_i) - I(x, y)), & \text{if } U(LBP_{P,R}) \leq 2 \\ P + 1, & \text{otherwise.} \end{cases} \quad (2.6)$$

Each rotation invariant “uniform” pattern is assigned a unique label equal to the number of ‘1’ in the pattern, while all the “non-uniform” patterns are labeled by  $P + 1$ . Therefore, there are  $P + 2$  different values for  $LBP_{P,R}^{riu2}$  and the final feature is the histogram of  $LBP_{P,R}^{riu2}$  accumulated over the entire image.

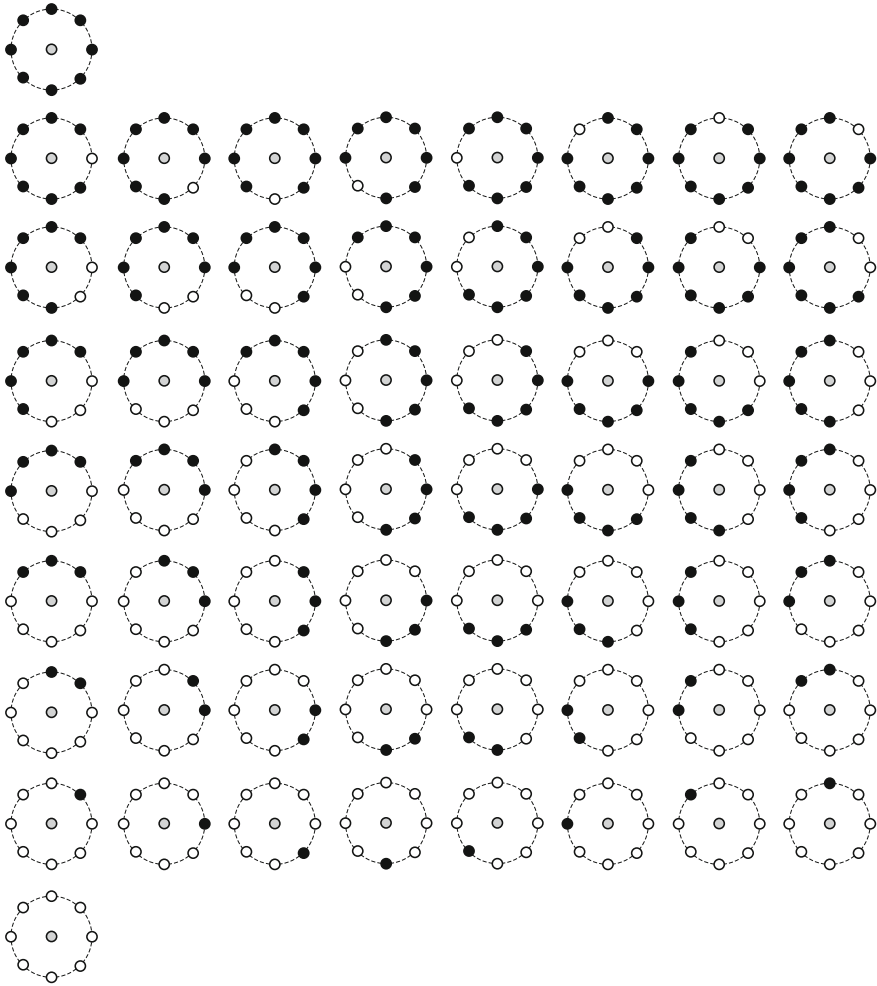


**Fig. 2.12** The different “uniform” patterns in the case of  $P = 8$ . The white circle denotes ‘1’ while the dark circle denotes ‘0’

### 2.2.1.2 Scale Invariant Feature Transform

SIFT is a local descriptor which is invariant to image translation, scaling and rotation, and partially invariant to occlusion/noise and change in illumination and view-point [32]. Lots of algorithms have been proposed recently that successfully utilize SIFT for image classification and object recognition [2, 10, 62, 64]. There are mainly four stages of computation involved in the generation of the SIFT feature described in the following sections.

### Scale-Space Extrema Detection

The first stage of computation is to identify the locations of candidate interest points which are invariant to orientation and scale change. A continuous function of scale, also named as scale space, is used to search stable features through all possible scales. It is verified that the Gaussian function is the only possible scale-space kernel [31], therefore the scale space of an image  $I$  can be generated by

$$L(x, y, \sigma) = G(x, y, \sigma) * I(x, y), \quad (2.7)$$

where  $G(x, y, \sigma) = \frac{1}{2\pi\sigma^2} \exp\left(-\frac{x^2+y^2}{2\sigma^2}\right)$  is a Gaussian function and  $*$  is the convolution operation.

The locations of stable keypoints in scale space are detected by using the extrema of the difference-of-Gaussian (DoG) function convolved with the original image. It can be formulated by

$$\begin{aligned} D(x, y, \sigma) &= (G(x, y, r\sigma) - G(x, y, \sigma)) * I(x, y) \\ &= L(x, y, r\sigma) - L(x, y, \sigma). \end{aligned} \quad (2.8)$$

An efficient way to generate  $D(x, y, \sigma)$  is illustrated in Fig. 2.13 [32]. Each octave of scale space is divided into  $t$  intervals ( $t$  should be an integer number) and  $r = 2^{1/t}$  is a multiplicative constant. The Gaussian image in next octave is the one in the

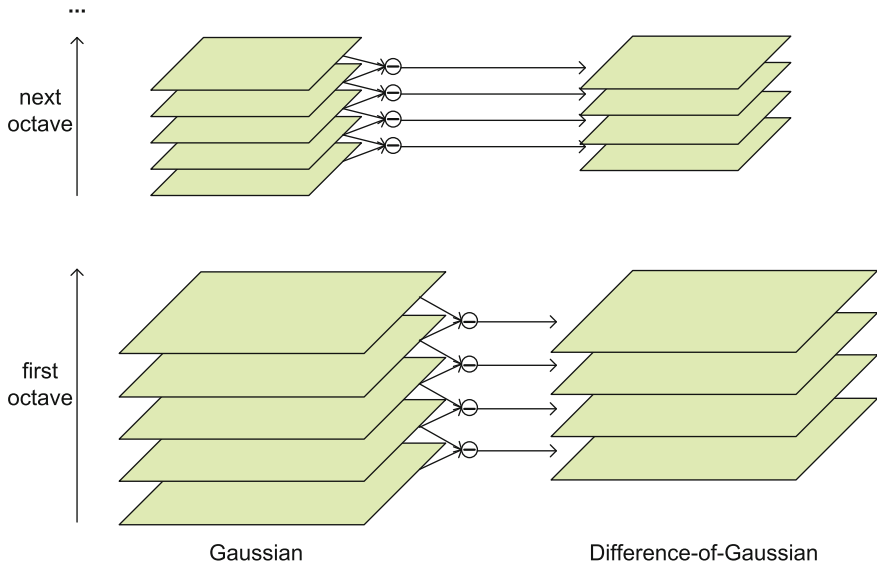


**Fig. 2.13** Construction of  $D(x, y, \sigma)$ . The scale space images are produced by convolving initial image incrementally with Gaussians. The DoG images are produced by subtracting adjacent Gaussian images

previous octave downsampled by a factor of 2. It is verified that we have to produce  $t + 3$  Gaussian images for each octave to insure that the extrema detection can cover the complete octaves. The DoG images are generated by subtracting adjacent blurred images.

To find the local extrema of the DoG images, each sample has to be compared to its 26 neighbors in  $3 \times 3$  regions of the DoG images at the current scale (eight neighbors), above scale (nine neighbors) and below scale (nine neighbors). Samples which are the maxima or minima among all of their neighbors are identified as the keypoint candidates.

### Keypoint Localization

After finding keypoint candidates, it is necessary to find stabile keypoints. It means that the points with low contrast and poor localization along the edges will be removed. It can be accomplished by using the Taylor expansion of the DoG image and the location of the extremum,  $\hat{\mathbf{x}}$ , can be determined by following formula [32]:

$$\hat{\mathbf{x}} = -\frac{\partial^2 D^{-1}}{\partial \mathbf{x}^2} \frac{\partial D}{\partial \mathbf{x}}, \quad (2.9)$$

where  $D$ ,  $\frac{\partial D}{\partial \mathbf{x}}$  and  $\frac{\partial^2 D}{\partial \mathbf{x}^2}$  are evaluated at the same selected point and  $\mathbf{x} = (x, y, \sigma)^\top$  is the offset from this point. It is worth noting that  $D$  is the Taylor expansion up to second order of original  $D(x, y, \sigma)$ .

The function value at the extremum  $D(\hat{\mathbf{x}})$  is calculated by

$$D(\hat{\mathbf{x}}) = D + \frac{1}{2} \frac{\partial D^\top}{\partial \mathbf{x}} \hat{\mathbf{x}}. \quad (2.10)$$

To reject the unstable extrema with low contrast, based on the experimental results in [32], those  $\hat{\mathbf{x}}$  with  $D(\hat{\mathbf{x}}) < 0.03$  is discarded.

To define the extreme points along the edges, a  $2 \times 2$  Hessian matrix is utilized as

$$H = \begin{bmatrix} D_{xx} & D_{xy} \\ D_{xy} & D_{yy} \end{bmatrix}, \quad (2.11)$$

where  $D_{xx}$ ,  $D_{xy}$  and  $D_{yy}$  is the second partial derivative of the DoG image.

To further eliminate the influence of the points localized along the edges, the candidate keypoints which are unable to satisfy following situation will be eliminated:

$$\frac{Tr(H)^2}{Det(H)} < \frac{(\gamma + 1)^2}{\gamma}, \quad (2.12)$$

where  $Tr(H)$  and  $Det(H)$  is respectively the trace and the determinant of matrix  $H$ .  $\gamma = 10$  is the ratio between the eigenvalue of  $H$  with the largest magnitude and the one with smaller magnitude.

### Orientation Assignment

Until now, the accurate keypoints are localized by removing the points with low contrast or along edges. The next step is to assign an orientation to each keypoint.

The gradient magnitude and orientation of the Gaussian smoothed image  $L(x, y)$ , which is obtained by using the scale  $\sigma$  of the keypoint, can be calculated by

$$m(x, y) = \sqrt{(L(x, y + 1) - L(x, y - 1))^2 + (L(x + 1, y) - L(x - 1, y))^2}, \quad (2.13)$$

$$\theta(x, y) = \tan^{-1} \left( \frac{L(x, y + 1) - L(x, y - 1)}{L(x + 1, y) - L(x - 1, y)} \right). \quad (2.14)$$

The orientations of sample points within a window around the keypoint are stored in one of 36 bins covering the  $360^\circ$ . Each point weighted by its gradient magnitude within a circular window with  $\sigma_w = 1.5\sigma$  around the keypoint, is added to the bin corresponding to the point's orientation. The highest peaks in the histogram is the dominant directions of the keypoint. Some other peaks with higher than 80 % of the highest one can also be used to create a keypoint with corresponding orientation. At last, a parabola is fitted to the three histogram values closest to each peak for generating the orientation with higher accuracy.

The location and orientation of keypoints in an image are shown in Fig. 2.14. By assigning orientation to each keypoint based on local image natures, the capability of invariance to image rotation can be obtained.

### Keypoint Descriptor

The location, scale and orientation has been assigned to each keypoint of an image. The last stage of the SIFT calculation is to create the descriptor, which should be highly distinctive and be partial invariant under differing illumination and viewpoint.

**Fig. 2.14** Keypoints detected in an image. The start point of *arrow* is the keypoint's location, the direction indicates the orientation of the local gradient at the keypoint and the length denotes the magnitude of the local gradient

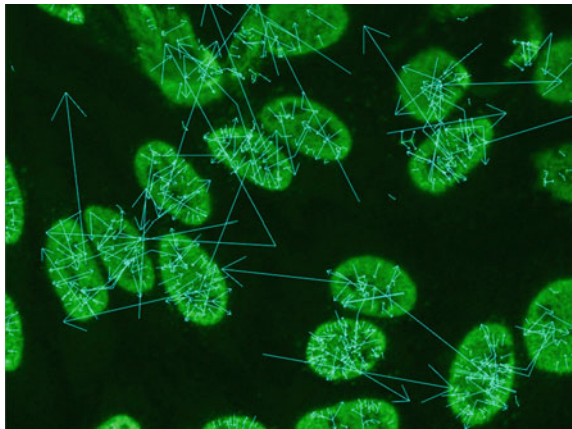
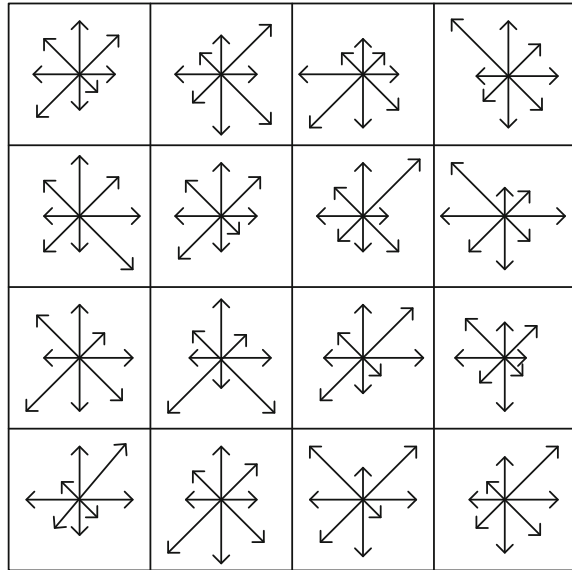


**Fig. 2.15** Keypoint descriptor



Firstly, the coordinates of the descriptor and the orientations of the local gradient are rotated relative to the orientation of keypoint to achieve orientation invariance. The gradient magnitude and orientation are sampled in a region of  $16 \times 16$  pixels around the keypoint. The magnitudes are weighted by a Gaussian window with a  $\sigma$  that is 1.5 times that of the circular descriptor window. Then, the orientation histograms over  $4 \times 4$  sample regions are calculated by accumulating the weighted magnitudes with nearly the same direction. Figure 2.15 shows a  $4 \times 4$  keypoint descriptor array with 8 orientation bins covering  $360^\circ$  in each. The length of each arrow is the sum of the gradient magnitudes of the samples near that orientation in the corresponding region. Since there are  $4 \times 4$  histogram arrays with 8 orientation bins, which is verified to show the best result [32], the dimension of the feature vector 128.

At last, the feature vector is normalized to unit length and the values in the unit feature vectors which are larger than 0.2 are changed to 0.2. Then the modified feature vectors are normalized again. The final feature vector achieves invariant to illumination with affine changes.

Therefore, the final SIFT features achieve orientation and scale invariance, partial illumination invariance and be stable when noise is added into the image.

### 2.2.2 Mid-Level Features

BoW framework and spatial pyramid matching (SPM) are two popular examples of mid-level features. The target of BoW framework is to embed low-level descriptors



in a representative codebook space. We introduce the key techniques employed in the BoW framework including SPM. First of all, low-level descriptors are firstly extracted at interest points or in dense grids. Then, a pre-defined codebook  $\mathbf{B}$  is applied to encode each descriptor using a specific coding scheme. The code is normally a vector with binary or continuous elements depends on coding scheme, which can be referred as mid-level descriptor. Next, the image is divided into increasingly finer spatial subregions. Multiple codes from each subregion are pooled together by averaging or normalizing into a histogram. Finally, the final image representation is generated by concatenating the histograms from all subregions together. There are two modules in the framework, i.e., coding and pooling.

- **Coding:** Local features of each image can be transformed to a collection of feature codes using a specific coding method. We compute a set of codes  $\mathbf{C} = \{\mathbf{c}_1, \mathbf{c}_2, \dots, \mathbf{c}_N\} \in \mathbb{R}^{M \times N}$  to represent the input local features  $\mathbf{X} = \{\mathbf{x}_1, \mathbf{x}_2, \dots, \mathbf{x}_N\} \in \mathbb{R}^{D \times N}$  by

$$\min_{\mathbf{C}} \sum_{i=1}^N \|\mathbf{x}_i - \mathbf{B}\mathbf{c}_i\|_{\ell_2}^2 + \lambda \mathcal{R}(\mathbf{x}_i) \quad (2.15)$$

where the first term measures the approximation error and the second one serves as a regularization term. We minimize information loss mainly by adjusting the regularization term.

- **Spatial Pooling:** The pooling procedure transforms mid-level features from an image into a final image representation. A crucial component which has great impact on pooling is SPM. It captures spatial layout information by expressing spatial relations at multiple levels of quantization. The codes within each spatial subregion are summarized by using a specific statistics strategy, such as the average of codes or their maximum.

## 2.3 Classification

Classification is the final and the most essential part for CAD systems. In this section, we introduce some basic classifiers applied for positive staining pattern classification.

### 2.3.1 Support Vector Machine

SVM classifier is one of the latest and most successful supervised learning classifiers and has been widely applied for image classification due to its efficiency. Using training labeled samples, a statistical model is constructed and then new samples can be classified according to this trained model. The linear SVM aims at searching

for an optimal hyperplane (or hyperplanes) in feature space with a large separating margin and a minimal misclassification rate.

For a binary linear SVM classifier, given training data and its corresponding labels  $(x_i, y_i)$ ,  $i = 1, 2, \dots, l$ ,  $x_i \in R^n$ ,  $y_i \in \{-1, +1\}$ , the concrete formulation can be defined by

$$\begin{aligned} \arg \min_{\mathbf{w}, \xi} \quad & \frac{1}{2} \mathbf{w}^\top \mathbf{w} + C \sum_{i=1}^l \xi_i, \\ \text{s.t.} \quad & y_i(\mathbf{w}^\top \mathbf{x}_i + b) \geq 1 - \xi_i, \quad \xi_i \geq 0 \quad \text{for } i = 1, 2, \dots, l. \end{aligned} \quad (2.16)$$

where  $C > 0$  is a penalty parameter to allow some misclassification and  $\xi_i$  are slack variables. The objective function aims to maximize the margin and the constraints indicate that the training points should be correctly classified by the relaxed decision function  $\mathbf{w}^\top \mathbf{x} + b$ . To extend binary SVM for multi-class problems, we use the *one-vs-all* approach [47]. We train a single binary SVM classifier per class by treating the cell images of this class as positive samples and those of other classes as negative samples. When classification is performed, all the binary classifiers are run and the classifier with the highest confidence score is chosen.

### 2.3.2 Nearest Neighbor Classifier

Traditional Nearest Neighbor Classifier (NNC) is one of the most commonly used and the simplest pattern classification methods yet devised [12]. It is a kind of statistic machine learning methods. We have  $N$  training sample pairs  $(x_i, y_i)$ ,  $i = 1, 2, \dots, N$ , where  $x_i$  is a set of features and  $y_i$  is class label. For a set of features  $x$  extracted from an image, it is desired to predict label  $y$  by utilizing the information contained in the set of training samples which are labeled correctly. A distance vector  $D = d_1, d_2, \dots, d_N$  is firstly calculated by  $d_i = \sqrt{(x - x_i)(x - x_i)^\top}$ . The  $l$ -th sample is the nearest neighbor of  $x$  if  $d_l = \min_i d_i$ . Therefore  $x$  is categorized into the class  $y_l$ .

$k$ -Nearest Neighbor algorithm ( $k$ NN) is also a simple classifier as a variant of NNC. Based on distance vector  $D$ ,  $k$  nearest neighbors of  $x$  with  $k$  smallest distances are obtained. Let the  $k$  nearest neighbors be  $\{(x'_1, y'_1), \dots, (x'_k, y'_k)\}$ ,  $x$  is assigned to class  $y$  according the majority voting among the labels  $y'_1, \dots, y'_k$ . The only parameter is  $k$  which should be chosen carefully. Generally, larger values of  $k$  reduce the effect of noise for classification and improve the classification performance, but they make the classes less distinct.

## References

1. Desmond Adler, Tony Ko, Paul Herz, and James Fujimoto. Optical coherence tomography contrast enhancement using spectroscopic analysis with spectral autocorrelation. *Optics express*, 12(22):5487–5501, 2004.
2. Danni Ai, Xianhua Han, Xiang Ruan, and Yen-Wei Chen. Adaptive color independent components based sift descriptors for image classification. In *Proceedings of the 2010 20th International Conference on Pattern Recognition*, pages 2436–2439. IEEE Computer Society, 2010.
3. Maria E Åkerman, Warren CW Chan, Pirjo Laakkonen, Sangeeta N Bhatia, and Erkki Ruoslahti. Nanocrystal targeting in vivo. *Proceedings of the National Academy of Sciences*, 99(20):12617–12621, 2002.
4. A Paul Alivisatos, Weiwei Gu, and Carolyn Larabell. Quantum dots as cellular probes. *Annu. Rev. Biomed. Eng.*, 7:55–76, 2005.
5. Roohollah Bagherzadeh, Masoud Latifi, Saeed Shaikhzadeh Najar, and Lingxue Kong. The application of cd se/zns quantum dots and confocal laser scanning microscopy for three-dimensional imaging of nanofibrous structures. *Journal of industrial textiles*, 43(4):496–510, 2014.
6. Byron Ballou, B Christoffer Lagerholm, Lauren A Ernst, Marcel P Bruchez, and Alan S Waggoner. Noninvasive imaging of quantum dots in mice. *Bioconjugate chemistry*, 15(1):79–86, 2004.
7. Marcel Bruchez, Mario Moronne, Peter Gin, Shimon Weiss, and A Paul Alivisatos. Semiconductor nanocrystals as fluorescent biological labels. *science*, 281(5385):2013–2016, 1998.
8. Victoria E Centonze. Introduction to multiphoton excitation imaging for the biological sciences. *Cell Biological Applications of Confocal Microscopy*, page 129, 2002.
9. Warren CW Chan and Shuming Nie. Quantum dot bioconjugates for ultrasensitive nonisotopic detection. *Science*, 281(5385):2016–2018, 1998.
10. Leonardo Chang, Miriam M Duarte, Luis Enrique Sucar, and Eduardo F Morales. A Bayesian approach for object classification based on clusters of sift local features. *Expert Systems With Applications*, 39(2):1679–1686, 2012.
11. Jui-Tai Chen, Ruei-Ming Chen, Yi-Ling Lin, Huai-Chia Chang, Yu-Hua Lin, Ta-Liang Chen, and Tyng-Guey Chen. Confocal laser scanning microscopy: 1. an overview of principle and practice in biomedical research. *ACTA ANAESTHESIOLOGICA SINICA*, 42:33–40, 2004.
12. Thomas M Cover and Peter E Hart. Nearest neighbor pattern classification. *Information Theory, IEEE Transactions on*, 13(1):21–27, 1967.
13. Maxime Dahan, Sabine Levi, Camilla Luccardini, Philippe Rostaing, Beatrice Riveau, and Antoine Triller. Diffusion dynamics of glycine receptors revealed by single-quantum dot tracking. *Science*, 302(5644):442–445, 2003.
14. Frank De Lange, Alessandra Cambi, Richard Huijbens, Bärbel de Bakker, Wouter Rensen, Maria Garcia-Parajo, Niek van Hulst, and Carl G Figdor. Cell biology beyond the diffraction limit: near-field scanning optical microscopy. *Journal of cell science*, 114(23):4153–4160, 2001.
15. Winfried Denk. Principles of multiphoton-excitation fluorescence microscopy. *Cold Spring Harbor Protocols*, 2007(10):pdb-top23, 2007.
16. Sulatha Dwarakanath, John G Bruno, Anant Shastri, Taylor Phillips, Ashely John, Ashok Kumar, and Larry D Stephenson. Quantum dot-antibody and aptamer conjugates shift fluorescence upon binding bacteria. *Biochemical and biophysical research communications*, 325(3):739–743, 2004.
17. Michael Edidin. Near-field scanning optical microscopy, a siren call to biology. *Traffic*, 2(11):797–803, 2001.
18. Justin Farlow, Daeha Seo, Kyle E Broaders, Marcus J Taylor, Zev J Gartner, and Young-wook Jun. Formation of targeted monovalent quantum dots by steric exclusion. *Nature methods*, 10(12):1203–1205, 2013.
19. MD Fricker and AJ Meyer. Confocal imaging of metabolism in vivo: pitfalls and possibilities. *Journal of experimental botany*, 52(356):631–640, 2001.

20. JM Girkin. Optical physics enables advances in multiphoton imaging. *Journal of Physics D: Applied Physics*, 36(14):R250, 2003.
21. Ralph Gräf, Jens Rietdorf, and Timo Zimmermann. Live cell spinning disk microscopy. In *Microscopy Techniques*, pages 57–75. Springer, 2005.
22. Weiwei Gu, Teresa Pellegrino, Wolfgang J Parak, Rosanne Boudreau, Mark A Le Gros, Daniele Gerion, A Paul Alivisatos, and Carolyn A Larabell. Quantum dot-based cell motility assay. *Science Signaling*, 2005(290):p15–p15, 2005.
23. Karl-Jürgen Halhuber and Karsten König. Modern laser scanning microscopy in biology, biotechnology and medicine. *Annals of Anatomy-Anatomischer Anzeiger*, 185(1):1–20, 2003.
24. Alan R Hibbs. *Confocal microscopy for biologists*. Springer Science & Business Media, 2004.
25. Barbara M Hoeling, Andrew D Fernandez, Richard C Haskell, Eric Huang, Whittier R Myers, Daniel C Petersen, Sharon E Ungersma, Ruye Wang, Mary E Williams, and Scott E Fraser. An optical coherence microscope for 3-dimensional imaging in developmental biology. *Optics Express*, 6(7):136–146, 2000.
26. Benoît Host, Laure Twyffels, Yves Roisin, and J-M Vanderwinden. Three-dimensional visualization of termite (apicotermitinae) enteric valve using confocal laser scanning microscopy. *Journal of microscopy*, 255(2):116–122, 2014.
27. Mark Howarth, Wenhao Liu, Sujiet Puthenveetil, Yi Zheng, Lisa F Marshall, Michael M Schmidt, K Dane Wittrup, Mouni G Bawendi, and Alice Y Ting. Monovalent, reduced-size quantum dots for imaging receptors on living cells. *Nature methods*, 5(5):397–399, 2008.
28. Anatoli Ianoul, Melissa Street, Donna Grant, John Pezacki, Rod S Taylor, and Linda J Johnston. Near-field scanning fluorescence microscopy study of ion channel clusters in cardiac myocyte membranes. *Biophysical journal*, 87(5):3525–3535, 2004.
29. Marjolein Koopman, Alessandra Cambi, Bärbel I de Bakker, Ben Joosten, Carl G Figdor, Niek F van Hulst, and Maria F Garcia-Parajo. Near-field scanning optical microscopy in liquid for high resolution single molecule detection on dendritic cells. *FEBS letters*, 573(1-3):6–10, 2004.
30. Blandine Laude, Antonello De Martino, Bernard Drevillon, Laurence Benattar, and Laurent Schwartz. Full-field optical coherence tomography with thermal light. *Applied optics*, 41(31):6637–6645, 2002.
31. Tony Lindeberg. Scale-space theory: A basic tool for analyzing structures at different scales. *Journal of applied statistics*, 21(1-2):225–270, 1994.
32. D.G. Lowe. Distinctive image features from scale-invariant keypoints. *Int. J. Comput. Vis.*, 60(2):91–110, 2004.
33. John N Mason, Ian D Tomlinson, Sandra J Rosenthal, and Randy D Blakely. Labeling cell-surface proteins via antibody quantum dot streptavidin conjugates. *Methods Mol Biol*, 303(1):35–50, 2005.
34. Sean G Megason and Scott E Fraser. Digitizing life at the level of the cell: high-performance laser-scanning microscopy and image analysis for in toto imaging of development. *Mechanisms of development*, 120(11):1407–1420, 2003.
35. Xavier Michalet, Fabien Pinaud, Thilo D Lacoste, Maxime Dahan, Marcel P Bruchez, A Paul Alivisatos, and Shimon Weiss. Properties of fluorescent semiconductor nanocrystals and their application to biological labeling. *Single Molecules*, 2(4):261–276, 2001.
36. Peter Mitchell. Turning the spotlight on cellular imaging. *Nature biotechnology*, 19(11):1013–1018, 2001.
37. Toshiyuki Miyashita. Confocal microscopy for intracellular co-localization of proteins. *Protein-Protein Interactions: Methods and Applications*, pages 399–409, 2004.
38. Christof M Niemeyer. Functional hybrid devices of proteins and inorganic nanoparticles. *Angewandte Chemie International Edition*, 42(47):5796–5800, 2003.
39. Timo Ojala, Matti Pietikäinen, and David Harwood. A comparative study of texture measures with classification based on featured distributions. *Pattern recognition*, 29(1):51–59, 1996.
40. Timo Ojala, Matti Pietikäinen, and Topi Maenpää. Multiresolution gray-scale and rotation invariant texture classification with local binary patterns. *Pattern Analysis and Machine Intelligence, IEEE Transactions on*, 24(7):971–987, 2002.

41. Aydogan Ozcan, Ertugrul Cubukcu, Alberto Bilenca, Kenneth B Crozier, Brett E Bouma, Federico Capasso, and Guillermo J Tearney. Differential near-field scanning optical microscopy. *Nano letters*, 6(11):2609–2616, 2006.
42. Stephen W Paddock. Principles and practices of laser scanning confocal microscopy. *Molecular biotechnology*, 16(2):127–149, 2000.
43. Jeremy S Paige, Thinh Nguyen-Duc, Wenjiao Song, and Samie R Jaffrey. Fluorescence imaging of cellular metabolites with rna. *Science*, 335(6073):1194–1194, 2012.
44. Matti Pietikäinen, Abdenour Hadid, Guoying Zhao, and Timo Ahonen. Local binary patterns for still images. In *Computer Vision Using Local Binary Patterns*, pages 13–47. Springer, 2011.
45. David W Piston. Imaging living cells and tissues by two-photon excitation microscopy. *Trends in cell biology*, 9(2):66–69, 1999.
46. K Reynaud, D Nogueira, R Cortvrindt, R Kurzawa, and J Smitz. Confocal microscopy: principles and applications to the field of reproductive biology. *Folia histochemica et cytobiologica/Polish Academy of Sciences, Polish Histochemical and Cytochemical Society*, 39(2):75–85, 2000.
47. Ryan Rifkin and Aldebaro Klautau. In defense of one-vs-all classification. *Mach. Learn. Res.*, 5:101–141, 2004.
48. Andrew Rollins, Siavash Yazdanfar, Manish Kulkarni, Rujchai Ung-Arunyawee, and Joseph Izatt. In vivo video rate optical coherence tomography. *Optics Express*, 3(6):219–229, 1998.
49. Sandra J Rosenthal. Bar-coding biomolecules with fluorescent nanocrystals. *Nature biotechnology*, 19(7):621–622, 2001.
50. Eleonora Ruocco, Giuseppe Argenziano, Giovanni Pellacani, and Stefania Seidenari. Noninvasive imaging of skin tumors. *Dermatologic surgery*, 30(s2):301–310, 2004.
51. Paul Selvin. New small quantum dots for neuroscience (presentation video). In *SPIE BiOS*, pages 89282X–89282X. International Society for Optics and Photonics, 2014.
52. Caroline Seydel. Quantum dots get wet. *Science*, 300(5616):80, 2003.
53. Andrei P Sommer and Ralf-Peter Franke. Near-field optical analysis of living cells in vitro. *Journal of proteome research*, 1(2):111–114, 2002.
54. AP Sommer and R-P Franke. Hydrophobic optical elements for near-field optical analysis (noa) in liquid environment—a preliminary study. *Micron*, 33(3):227–231, 2002.
55. Martin Straub and Stefan W Hell. Multifocal multiphoton microscopy: a fast and efficient tool for 3-d fluorescence imaging. *Bioimaging*, 6(4):177–185, 1998.
56. Mitsuro Sugita, Michael Pircher, Stefan Zotter, Bernhard Baumann, Kenichi Saito, Tomoyuki Makihira, Nobuhiro Tomatsu, Makoto Sato, and Christoph K Hitztenberger. Analysis of optimum conditions of depolarization imaging by polarization-sensitive optical coherence tomography in the human retina. *Journal of biomedical optics*, 20(1):016011–016011, 2015.
57. DJ Taatjes, CJ Palmer, C Pantano, S Buder-Hoffmann, A Cummins, and BT Mossman. Laser-based microscopic approaches: application to cell signaling in environmental lung disease. *Biotechniques*, 31(4):880–895, 2001.
58. Wee Beng Tan and Yong Zhang. Surface modification of gold and quantum dot nanoparticles with chitosan for bioapplications. *Journal of biomedical materials research Part A*, 75(1):56–62, 2005.
59. Fuyuki Tokumasu, Rick M Fairhurst, Graciela R Ostera, Nathaniel J Brittain, Jeeseong Hwang, Thomas E Wellems, and James A Dvorak. Band 3 modifications in plasmodium falciparum-infected aa and cc erythrocytes assayed by autocorrelation analysis using quantum dots. *Journal of cell science*, 118(5):1091–1098, 2005.
60. Pavel Vesely and Alan Boyde. Fast intracellular motion in the living cell by video rate reflection confocal laser scanning microscopy. *Journal of anatomy*, 198(6):641–649, 2001.
61. Tie Xia, Nan Li, and Xiaohong Fang. Single-molecule fluorescence imaging in living cells. *Annual review of physical chemistry*, 64:459–480, 2013.
62. Xiang Xu, Feng Lin, Carol Ng, and Khai Pang Leong. Staining pattern classification of anafif based on sift features. *Journal of Medical Imaging and Health Informatics*, 2(4):419–424, 2012.

63. Dvir Yelin and Yaron Silberberg. Laser scanning third-harmonic-generation microscopy in biology. *Optics express*, 5(8):169–175, 1999.
64. Huiyu Zhou, Yuan Yuan, and Chunmei Shi. Object tracking using sift features and mean shift. *Computer vision and image understanding*, 113(3):345–352, 2009.

Cellular Image Classification

Xu, X.; Wu, X.; Lin, F.

2017, IX, 137 p. 60 illus., Hardcover

ISBN: 978-3-319-47628-5